


Characterization of an atom interferometer in the quasi-Bragg regime

A. Béguin, T. Rodzinka, J. Vigué , B. Allard, and A. Gauguet *

Laboratoire Collisions Agrégats Réactivité, Université Paul Sabatier, 118 route de Narbonne, 31062 Toulouse Cedex 4, France

 (Received 2 December 2021; revised 14 February 2022; accepted 15 February 2022; published 2 March 2022)

We provide a comprehensive study of ultracold-atom diffraction by an optical lattice. We focus on an intermediate regime between the Raman-Nath and Bragg regimes, the so-called quasi-Bragg regime. The experimental results are in good agreement with a full numerical integration of the Schrödinger equation. We investigate the long-pulse regime limited by a strong velocity selection and the short-pulse regime limited by “nonadiabatic losses.” For each of these regimes, we estimate the multipoint features of the Bragg interferometers. Finally, we discuss the best compromise between these two regimes, considering the diffraction phase shift and the existence of parasitic interferometers.

DOI: [10.1103/PhysRevA.105.033302](https://doi.org/10.1103/PhysRevA.105.033302)

I. INTRODUCTION

In 1933, Kapitza and Dirac [1] proposed the diffraction of electrons by a standing light wave to study the stimulated emission process. Because of the weakness of the interaction between free electrons and photons, the first convincing experimental observation was not performed until 2001 [2]. However, an atomic analog of the Kapitza-Dirac effect was proposed by Althuler *et al.* [3], who pointed out the huge enhancement of the diffraction probability if one replaces electrons by atoms and if one uses quasiresonant laser radiation. Following this idea, atomic diffraction by a standing light wave was demonstrated in the 1980s [4,5].

These seminal works led to a number of experimental and theoretical studies [6–12]. In particular, two extreme regimes of diffraction are useful for discussions: the Raman-Nath and Bragg regimes [13,14]. The Raman-Nath regime corresponds to a short and intense atom-light interaction. In this regime, the scattering process leads to the population of many atom momentum states. On the other hand, a long interaction time and a shallow optical potential give rise to the Bragg regime [15], where only a single diffraction order is allowed by energy conservation. It provides efficient and adjustable two-port beam splitters which are required for implementing two-path interferometer geometries. These interferometers are of great interest for accurate interferometric measurements as they allow a straightforward readout of the atomic phase shift.

Although most of the precision measurements in atom interferometry use two-photon Raman beam splitters [16–23], Bragg scattering has several attractive features for atom interferometry. First, in a Bragg interferometer, the atoms propagate in the same internal state, which makes the atomic phase less sensitive to external fields. This property could be advantageous for accurate inertial sensors [24]. Interferometers with a single internal state are also important for accurate

measurements of some atomic properties [25] or geometrical phase shifts [26,27]. Furthermore, the high-order Bragg diffraction allows an increase of the separation between the interferometer arms and hence the interferometer sensitivity. The first atom interferometer based on Bragg diffraction was demonstrated by Giltner *et al.* [28] with a momentum separation of up to six photon recoils ($6\hbar k$).

High-order diffraction in the Bragg regime [29,30] requires a very long atom-optical lattice interaction time which is difficult to handle in interferometric measurements. Nevertheless, in the area between the Raman-Nath and Bragg regimes, the so-called quasi-Bragg regime, it is possible to achieve an effective two-port beam splitter using a smooth temporal profile of the optical lattice intensity [13,31,32]. Using a Gaussian shape pulse, Müller *et al.* [33] performed the atom interferometer with the highest diffraction order ($24\hbar k$). A convenient description of the quasi-Bragg regime relies on the adiabatic following of eigenstates [13,31,34,35]. Taking full advantage of the adiabatic theorem, Siemß *et al.* [35] demonstrated an analytical formalism describing losses and phase shifts for a sharp momentum distribution.

Many efforts have been made to further increase the number of photon recoils transferred to the atom in order to produce large-momentum-transfer (LMT) beam splitters. Different processes were demonstrated; most of them create a superposition of two momentum states using a first diffraction pulse followed by an acceleration of each state with a sequence of diffraction pulses [36–39] or Bloch oscillations in an accelerated optical lattice [40–43]. Recent years have seen spectacular breakthroughs in the development of LMT interferometers, demonstrating coherence for up to $408\hbar k$ [44]. The LMT beam splitters are one of the main prospects for the improvement of inertial sensor technologies [45,46] and fundamental constant measurements [38,47]. The LMT beam splitters are also central for new tests in gravitational physics [48–53]. In addition, interferometers with a very large spatial separation [54,55] pave the way for measurements in which the macroscopic separation between the two arms is essential, for example, in cavity QED [56], entangled state

*gauguet@irsamc.ups-tlse.fr

engineering [57], and measurements such as Aharonov-Bohm related phases [58–60].

A thorough understanding of the quasi-Bragg scattering is fundamental for metrology with LMT atom interferometers. In particular, the complex dynamics of the nonresonant momentum states leads to diffraction phase shifts [32,35,61] and multiple interferometers [24,62] which are crucial for determining the fundamental limits of the sensitivity and the accuracy. Theoretical approaches based on perturbative expansion allow a qualitative description of the diffraction phases in the quasi-Bragg regime [32]. However, a more quantitative description needs to consider the momentum distribution of the atomic ensemble [35,63].

In this paper, we investigate experimentally the interplay between diffraction efficiency, diffraction phase, and multiport beam splitters which were explored theoretically in [32,35,63]. We measure the Rabi oscillations between the Bragg states and the nonadiabatic losses for high-order diffraction at finite momentum width. The very good agreement with numerical simulations allows a quantitative understanding of the diffraction dynamics and the diffraction phases. We demonstrate a short-pulse (SP) regime and a long-pulse (LP) regime within the quasi-Bragg regime. In the SP regime a complex dynamics is induced by large nonadiabatic losses, while in the LP regime the evolution merges the effective two-level model at a high Rabi cycle ($\geq \pi$). An optimal efficiency is found at the border between these two regimes. We also present the interference patterns for multiport interferometers operating in the quasi-Bragg regime. The fringe patterns of each output port of the interferometer are compared with numerical simulations. This allows us to anticipate further experimental and theoretical studies regarding the inherent diffraction phase shifts and multiport features of LMT interferometers based on quasi-Bragg diffraction.

This paper is organized as follows: Sec. II presents general aspects of atom diffraction in the quasi-Bragg regime and the numerical model we use to analyze the experimental results. Section III discusses the experimental diffraction patterns and the interferometers signals in the quasi-Bragg regime.

II. ATOM DIFFRACTION MODEL

We consider a Bose-Einstein condensate (BEC) interacting with a vertical optical lattice created by two counterpropagating laser beams with a frequency difference $\Delta\omega = \omega_1 - \omega_2$. The mean wave number of the two running waves is denoted $k = \frac{\omega_1 + \omega_2}{2c}$. The laser is far detuned from the resonant absorption frequencies, allowing an adiabatic elimination of the excited internal state. Therefore, the atom-light interaction reduces to a light shift, proportional to the light intensity, leading to the potential $2\hbar\Omega \sin^2(kz)$, where Ω is the two-photon Rabi frequency (see Appendix A).

In our experiments, we use an expanded BEC source in which atom-atom interactions are negligible. Therefore, the evolution of the BEC is completely described by a single-atom Hamiltonian H including the kinetic energy, the gravitational potential, and the periodic light shift. In the laboratory frame,

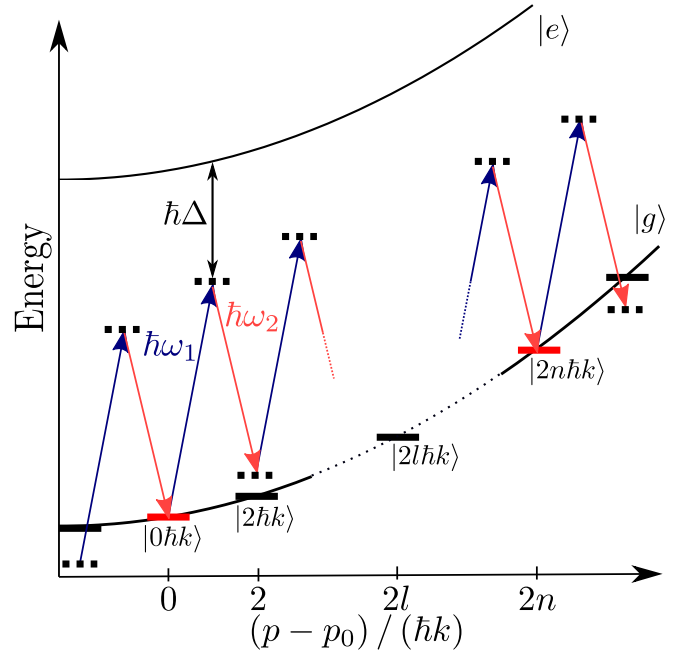


FIG. 1. Energy-momentum parabolic dispersion relation. The Bragg order n diffraction process can be interpreted as multiple two-photon processes between an input state in momentum $|p_0\rangle$ and an output momentum state $|p_0 + 2n\hbar k\rangle$. The two laser beams forming the optical lattice have frequencies ω_1 and ω_2 detuned by Δ with respect to the atomic transition.

the Hamiltonian is written

$$H = \frac{\hat{p}^2}{2M} + Mg\hat{z} + 2\hbar\Omega(t) \sin^2 \left[k\hat{z} - \frac{\phi(t)}{2} \right], \quad (1)$$

where M is the mass of the atom and \hat{z} and \hat{p} are the position and momentum operators along the direction of the optical lattice. $\phi(t)$ is the phase difference between the two laser running waves of the optical lattice. Using the unitary operator $U = e^{\frac{i}{\hbar} \frac{Mg^2 t^3}{6}} e^{\frac{i}{\hbar} \frac{\phi(t)}{2k} \hat{p}} e^{\frac{i}{\hbar} Mg\hat{z}t}$, we transform the Hamiltonian to $\tilde{H} = UHU^\dagger + i\hbar\dot{U}U^\dagger$, corresponding to a free-falling frame, and in this Hamiltonian, the gravitational potential does not appear explicitly:

$$\tilde{H} = \frac{\hat{p}^2}{2M} - \hat{p} \left(\frac{\dot{\phi}}{2k} + gt \right) + \hbar\Omega(t) - \frac{\hbar\Omega(t)}{2} (e^{2ik\hat{z}} + e^{-2ik\hat{z}}). \quad (2)$$

The operators $e^{\pm 2ik\hat{z}}$ couple atomic states differing by two photon momenta. Therefore, the periodic potential is interpreted as a two-photon process in which a photon is absorbed from one running wave and reemitted into the other one with a transfer of two photon momenta $2\hbar k$. The two-photon process can occur n times and transfer $2n$ photon momenta corresponding to higher diffraction orders, as illustrated in Fig. 1. Hence, it is convenient to expand the wave function on the plane waves $|2l\hbar k\rangle$: $|\Psi\rangle = \sum_{l=-m}^{n+m} A_l |2l\hbar k\rangle$, where A_l are the complex amplitudes of the plane-wave decomposition (see Fig. 1). We truncate the basis considering $2m$ outer states surrounding the two Bragg states $|0\hbar k\rangle$ and $|2n\hbar k\rangle$ and the states in between them. In this basis, the Hamiltonian $\tilde{H}(t)$ is

written as a tridiagonal matrix:

$$\begin{aligned} & \tilde{H}(t) \\ & = 4\hbar\omega_r \begin{pmatrix} \delta_{-m} & \gamma(t) & 0 & \dots & \dots & \dots & 0 \\ \gamma(t)^* & \ddots & \ddots & \ddots & \ddots & \ddots & \vdots \\ 0 & \ddots & 0 & \ddots & \ddots & \ddots & \vdots \\ \vdots & \ddots & \ddots & \ddots & \ddots & \ddots & \vdots \\ \vdots & \ddots & \ddots & \ddots & \delta_n & \ddots & 0 \\ \vdots & \ddots & \ddots & \ddots & \ddots & \ddots & \gamma(t) \\ 0 & \dots & \dots & \dots & 0 & \gamma(t)^* & \delta_{n+m} \end{pmatrix}, \end{aligned} \quad (3)$$

where $\omega_r = \frac{\hbar k^2}{2M}$ is the recoil frequency of a single photon and $\gamma(t) = \frac{\Omega(t)}{8\omega_r}$ is the dimensionless effective two-photon Rabi frequency $\Omega(t)$. The diagonal terms $\delta_l(t) = l^2 - l\tilde{v}(t)$ depend on the usual kinetic energy in l^2 and on the velocity $\tilde{v}(t)$ of the lattice with respect to the free-falling atoms (in units of $\frac{\hbar k}{M}$):

$$\tilde{v}(t) = \frac{v(t) + (gt - v_0)}{v_r} = \frac{\Delta\omega(t)}{4\omega_r} + \frac{(gt - v_0)}{v_r}. \quad (4)$$

v_0 is the initial atom velocity in the lattice direction in the laboratory frame. In addition, the lattice velocity is set by the frequency difference $\Delta\omega$ in between the two beams. A time-dependent frequency ramp $\Delta\omega(t) = \omega_0 + \alpha t$, with $\alpha t = -2kgt$, is adjusted to cancel out the Earth acceleration so that the Bragg condition is always verified. The constant value $\omega_0 = 4n\omega_r + 2kv_0$ cancels out the diagonal term δ_n and defines the Bragg condition at order n for a given v_0 .

The Schrödinger equation leads to a system of differential equations. Approximate solutions exist, in particular for rectangular pulse shapes of the lattice amplitude. Two extreme cases are widely discussed in the literature [12]. The first case corresponds to short enough interaction times to neglect the dynamics of the external states, i.e., for short interaction times compared to the period of classical oscillation in the optical potential $\tau < (8\omega_r\sqrt{|\gamma|})^{-1}$. This approximation corresponds to the Raman-Nath approximation [64], introduced for the diffraction of light by high-frequency sound waves, now used in acousto-optic devices [65,66]. The broad spectrum associated with a short rectangular pulse leads to multiple diffraction orders and is poorly suited for atom beam splitters. On the other hand, the Bragg regime corresponds to the interaction with a weak potential: $|\gamma| \ll 1$. The population in the nonresonant momentum states vanishes, and they can be ignored in a perturbative approximation. The result is a two-level system leading to Rabi oscillations between the diffracted states.

A rough estimate of the effective Rabi frequency for diffraction of order n is given by the first nonzero term of the perturbation expansion [29]: $\Omega_n \approx \frac{\Omega^n}{(8\omega_r)^{n-1}(n-1)!^2}$. This result is not accurate as soon as Ω_n is not very small with respect to ω_r ; the higher terms of the perturbation expansion are then no longer negligible. However, this quantity is proportional to the difference of the a_n and b_n coefficients of the Mathieu equation [67], and it is well established that the power expansions of these coefficients have a rather small radius of convergence [68], so that the convergence of the perturbation expansion of Ω_n is slow. Despite its inaccuracy the approximate formula

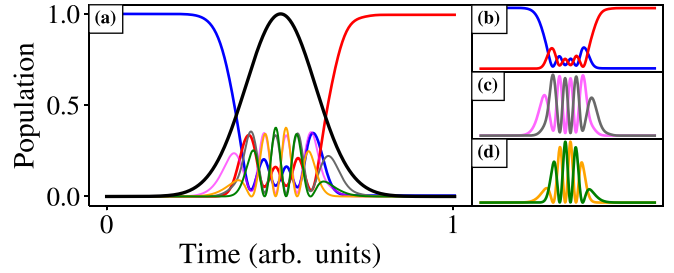


FIG. 2. (a) Evolution of the populations during a Gaussian pulse for Bragg order $n = 3$. The solid black line represents the Gaussian pulse amplitude as a function of time. The pulse duration $\sigma = \omega_r^{-1}$ and the maximum amplitude $\gamma_{\max} = 3.3$ were chosen to produce a perfect Bragg mirror. Populations are plotted in (b) for the two Bragg states ($|0\hbar k\rangle$ in blue and $|6\hbar k\rangle$ in red) and in (c) and (d) for the unwanted states. Inner states ($|2\hbar k\rangle$ in pink and $|4\hbar k\rangle$ in gray) in (c) and outer states ($|-2\hbar k\rangle$ in yellow and $|8\hbar k\rangle$ in green) in (d) oscillate by pair.

for Ω_n illustrates the necessity of high laser power and a very long interaction for large values of the Bragg order n . Therefore, the Bragg regime is not of practical interest for high momentum transfer.

We are interested in the intermediate regime introduced by Müller *et al.* [32] and named the quasi-Bragg regime. This regime has shown efficient high-order Bragg diffraction for an experimentally accessible set of parameters. The regime occurs when the potential is switched on and off smoothly. As for the Bragg diffraction, in the quasi-Bragg regime two output momentum states are mainly populated once the pulse has ended. In the analytical theory developed in [35] the finite momentum dispersion is described perturbatively, and the losses act as small corrections to the description of the quasi-Bragg diffraction process. As the parameters of our experiments are beyond these approximations, we study the dynamics by numerically solving the Schrödinger equation in the free-falling frame using the discrete momentum basis. The populations on each momentum state are calculated as the squared complex amplitudes after the interaction with the lattice: $P_l = A_l^2$. In what follows, we use a Gaussian pulse of the lattice amplitude to reduce losses in unwanted states [32,63]:

$$\gamma(t) = \gamma_{\max} \exp\left[-\frac{t^2}{2\sigma^2}\right], \quad (5)$$

where σ is the Gaussian pulse duration and γ_{\max} is the amplitude (peak two-photon Rabi frequency). The numerical propagation is performed on a 10σ time window centered on the pulse.

Figure 2 illustrates the time evolution of the populations in the momentum states during a Gaussian pulse of Bragg order $n = 3$ and for zero velocity dispersion. The pulse parameters are set to realize a perfect mirror pulse in which only the Bragg state $|6\hbar k\rangle$ is populated at the end of the pulse.

If the Bragg condition is fulfilled, the two Bragg states are two eigenstates and are degenerate at the start of the interaction ($|\gamma| \ll 1$). When the amplitude of the lattice increases sufficiently slowly, the populations adiabatically follow these two eigenstates. At the end of the pulse, the two eigenstates

return back to the initial two momentum states leading to Rabi oscillations. The weight in each Bragg state depends on the accumulated phase (Rabi phase θ_R) during the evolution. For the calculation, we use the momentum basis, which is not the eigenbasis of the system (Bloch states) in the presence of the lattice. The adiabatic following of the two eigenstates corresponds to the oscillation of unwanted momentum states by pairs with a non-negligible amplitude which finally destructively interfere.

The complex dynamics between momentum states during the pulse is a signature of the quasi-Bragg regime. It emphasizes the importance of considering the inner states ($0 < l < n$) and some outer states ($l < 0$ and $l > n$) to accurately describe the complete evolution of the atomic populations. The number $2m$ of outer states to be considered is linked to the spectral width of the pulse, so it depends on the Bragg order n , the pulse duration σ , and the pulse amplitude γ_{\max} . Appendix B discusses a criterion for the minimum number of outer states to be taken into account in (3) to ensure the convergence of our simulations.

In the quasi-Bragg regime, changing the pulse duration for a given amplitude does more than drive Rabi oscillations between the two Bragg states. Figure 3(a) shows the evolution of the populations in the different relevant states at the end of a pulse of duration σ for $\gamma_{\max} = 3.3$. Two subregimes can be distinguished: the SP regime, where many unwanted states are populated, and the LP regime, where the population oscillates between the two Bragg states. In the LP regime, the oscillation between these two states is well predicted by a two-level calculation despite the fact that unwanted states are transiently populated during the pulse. It is interesting to notice that in the SP regime the populations in the unwanted states, i.e., the losses, synchronously cancel out for specific values of σ . This cancellation offers the opportunity to experimentally choose pulse parameters that exploit the loss cancellation in the SP regime to maximize the diffraction efficiency. In what follows, the diffraction efficiency refers to a mirror pulse, and it is measured as the fraction of the population transferred in $|2n\hbar k\rangle$, i.e., P_n .

The boundary between the SP regime and the LP regime and the periodic cancellation of the losses are illustrated in Fig. 4. Figure 4 presents the total population in the two Bragg states in a σ - γ_{\max} map for Bragg order $n = 3$. The SP and LP regimes are clearly identified. The boundary is pushed towards longer pulses as γ_{\max} increases. It follows the intuitive picture that the spectral width increases with γ_{\max} and needs to be compensated by a longer pulse to maintain the adiabaticity of the pulse. The actual shape of the boundary is, however, nontrivial since it relies on multiple interferences between unwanted states. It also appears that the loss cancellation presents a periodic pattern that can be interpreted as Stückelberg interferometers [69]. Stückelberg interferences are due to the symmetry of the Gaussian pulse, which induces a symmetric series of avoided crossings between the rising part and the falling part of the pulse. Each avoided crossing acts as a beam splitter for the eigenstates which splits and recombines the wave functions. The resulting interferometers lead to oscillations between the Bragg states and the losses that depend on the phase difference due to the

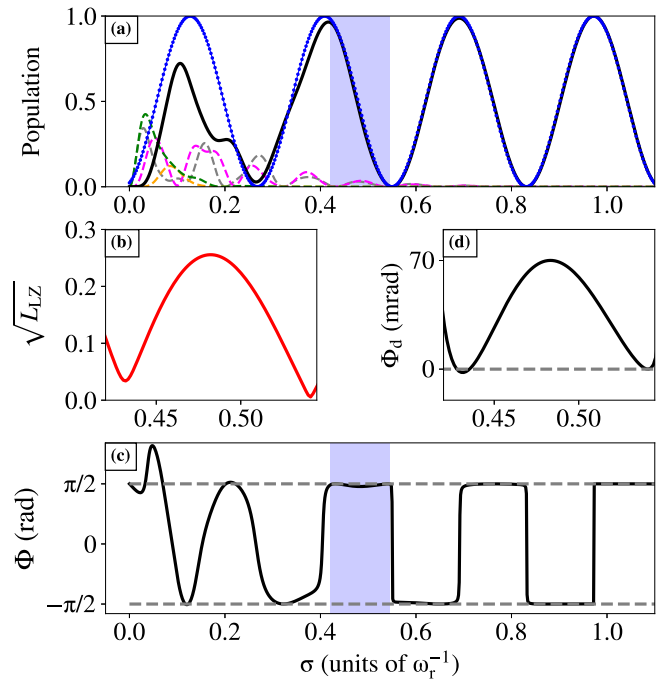


FIG. 3. Numerical simulation of diffraction at order $n = 3$ in the quasi-Bragg regime with zero velocity dispersion and $\gamma_{\max} = 3.3$. (a) Evolution of populations in the different momentum states as a function of the pulse duration σ ; the population of the initial state $|0\hbar k\rangle$ is not plotted. The black solid line represents the population in the diffracted Bragg state $|6\hbar k\rangle$; the populations in the unwanted states are plotted as dashed lines. The blue dotted line is the result of an effective two-level calculation for the population in the $|6\hbar k\rangle$ state. It overlaps with the numerical calculation in the long-pulse (LP) regime and shows that the Rabi phase θ_R is continuously built from the short-pulse (SP) regime. (b) Square root of the total population in the unwanted states for a pulse duration around $0.5\omega_r^{-1}$ [shaded regions in (a) and (c)]. (c) Diffraction phase Φ as a function of σ . The two gray dashed lines indicate constant $\pm\pi/2$ phases. They match the diffraction phase calculated in the LP regime. (d) Diffraction phase compensated from the trivial $\pi/2$ contribution ($\Phi_d = \Phi - \pi/2$) for the same pulse duration.

propagation in the different eigenstates. Following [35], we call these losses due to nonadiabatic effect Landau-Zener (LZ) losses L_{LZ} .

The diffraction efficiency is not the only relevant parameter when we plan to use Bragg diffraction to build an atom interferometer. The diffracted waves are imprinted with a phase that needs to be controlled at a metrological level. The numerical calculation gives access to the diffraction phase Φ between the two Bragg states as the difference between the arguments of the complex amplitudes after the pulse: $\Phi = \arg A_n - \arg A_0$.

Figure 3(c) represents the relative phase Φ as a function of σ for $\gamma_{\max} = 3.3$. In the LP regime, the diffraction phase oscillates as expected in the deep Bragg regime (effective two-level approximation); that is, the phase Φ jumps between $\pm\pi/2$ for each half period. However, in the SP regime, we observe a complex phase evolution highlighting the link between diffraction phase and LZ losses [32,35]. Müller *et al.* [32] showed that the nontrivial phase Φ_d is bounded by $\Phi_d \leq$

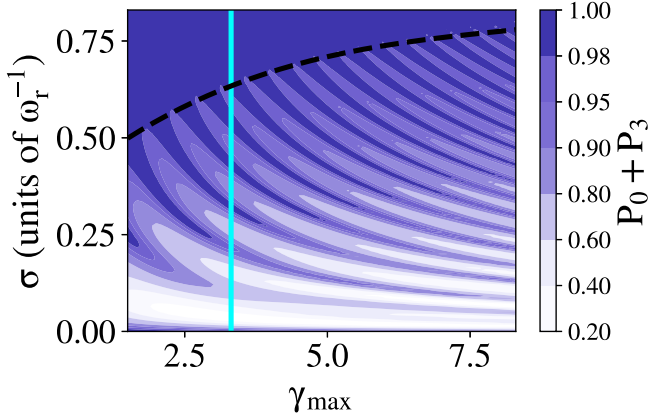


FIG. 4. The total population $P_0 + P_3$ of the two Bragg states ($|0\hbar k\rangle$ and $|6\hbar k\rangle$) in color scale in a σ - γ_{\max} map for $n = 3$. The calculation assumes a vanishing velocity dispersion. The black dashed line is a guide to the eye showing the boundary between the SP and LP regimes. The light blue solid line corresponds to the cut at $\gamma_{\max} = 3.3$ studied in Fig. 3.

$\sqrt{L_{\text{LZ}}}$. Figures 3(b) and 3(d) present, respectively, the square root of the losses and Φ_d for $\sigma \in [0.37\omega_r^{-1}, 0.52\omega_r^{-1}]$ close to the LP regime boundary where the losses are small. In this range, $\Phi_d \approx \sqrt{L_{\text{LZ}}}/3$, confirming that the vanishing losses coincide with a minimum of nontrivial diffraction phase.

To reproduce experimental data as accurately as possible, the finite velocity dispersion of the atomic cloud has to be taken into account in the calculation as the diagonal matrix elements explicitly depend on the atom velocity. This is done by adding to the lattice velocity $\tilde{v}(t)$ used in Eq. (4) a random variable $\delta\tilde{v}$ following the Gaussian distribution:

$$\rho(\delta\tilde{v}) = \frac{1}{\sqrt{2\pi\sigma_v^2}} \exp\left[-\frac{\delta\tilde{v}^2}{2\sigma_v^2}\right], \quad (6)$$

where σ_v is a Gaussian width proportional to the atomic cloud velocity dispersion. The numerical calculation is performed for each velocity class, and the mean atomic population in each momentum state is the weighted average over the distribution.

The main consequence of a finite velocity dispersion is to reduce the diffraction efficiency for long pulses as part of the atomic distribution ends up being off resonant. From this point of view, one would like to compromise on the pulse duration to minimize both Landau-Zener losses and velocity selection losses [63]. The existence of this compromise is illustrated in Fig. 5, taking as an example diffraction order $n = 3$ with a velocity dispersion of $0.32v_r$, which is relevant to our experiment (see Sec. III). The right part of Fig. 5 maps the population in the diffracted Bragg state $|6\hbar k\rangle$ in a σ - γ_{\max} plane. It presents a series of local maxima corresponding to Rabi phases that match odd multiples of π . The left part of Fig. 5 shows the evolution of the transferred population as a function of the pulse duration along the local maximum lines drawn by dashed lines in the σ - γ_{\max} plane. Each curve corresponds to a given Rabi phase ($\theta_R = \pi, 3\pi$, etc.). All the odd- π Rabi phases in the LP regime reach a similar maximum transfer efficiency for a given $(\sigma, \gamma_{\max})_{\text{opt}}$. This optimal

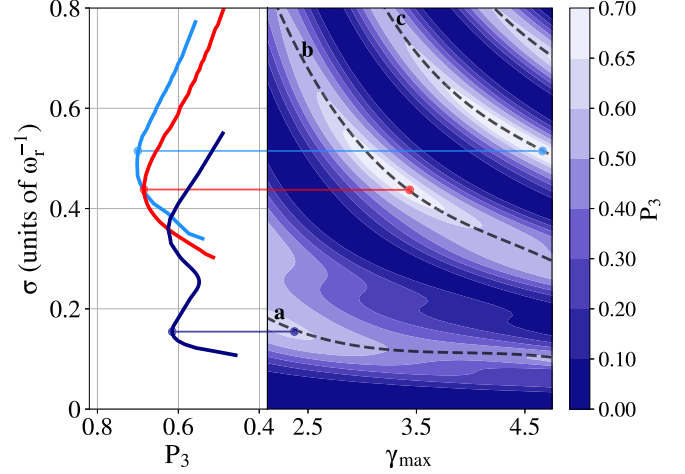


FIG. 5. Population P_3 in the diffracted Bragg state for $n = 3$. The calculation takes into account a velocity dispersion of $0.32v_r$. Right: Diffracted population P_3 in a color scale in a σ - γ_{\max} map. Dashed lines are guides to the eye showing local maximum lines achieving Rabi phases $\theta_R = \pi$ (dashed line a), 3π (dashed line b), 5π (dashed line c), etc. Left: Diffracted population along maxima lines. The dark blue curve corresponds to $\theta_R = \pi$, the red curve corresponds to $\theta_R = 3\pi$, and the light blue curve corresponds to $\theta_R = 5\pi$. An optimal transfer is realized for well-chosen $(\sigma, \gamma_{\max})_{\text{opt}}$ couples for $\theta_R \geq 3\pi$.

transfer is limited by the velocity selection losses, which are similar for all $(\sigma, \gamma_{\max})_{\text{opt}}$. In this example, the maximum efficiency can be reached for $\theta_R \geq 3\pi$. An interesting trade-off is the pulse duration $\sigma_{\text{opt}} \simeq 0.4\omega_r^{-1}$ corresponding to $\theta_R = 3\pi$, which minimizes the peak Rabi frequency. Going for a higher Rabi phase with equivalent efficiency would further reduce Landau-Zener losses, but it would increase negative effects scaling with $\sigma\gamma_{\max}$ such as spontaneous emission losses and phases related to ac Stark shifts.

In the next section we numerically and experimentally investigate the impact of finite temperature on high-order diffraction beam splitters in the quasi-Bragg regime.

III. EXPERIMENTAL RESULTS

A. Experimental setup

The atomic source is an evaporatively cooled ^{87}Rb ensemble in a crossed dipole trap in the presence of a magnetic field gradient to purify the ensemble in the magnetically insensitive Zeeman sublevel of the lower hyperfine state $|F = 1, m_F = 0\rangle$. We obtain a BEC of $N = 8 \times 10^4$ atoms with final trapping frequencies $(60 \times 900 \times 1100) \text{ Hz}^3$. The single-shot velocity dispersion is further reduced by transferring the BEC in a much shallower trap $(10 \times 80 \times 80) \text{ Hz}^3$, leading to a velocity dispersion of about $0.32 \pm 0.05v_r = 1.9 \pm 0.3 \text{ mm s}^{-1}$, with $v_r \sim 5.9 \text{ mm s}^{-1}$, including center-of-mass velocity fluctuations.

The vertical optical lattice used for Bragg diffraction is sketched in Fig. 6. The laser source is a 1560-nm-laser frequency doubled to 780 nm with a detuning $\Delta = 11 \text{ GHz}$ from the ^{87}Rb $|5S_{1/2}, F = 1\rangle$ to $|5P_{3/2}, F' = 2\rangle$ transition. This detuning is sufficient to ensure negligible spontaneous emission

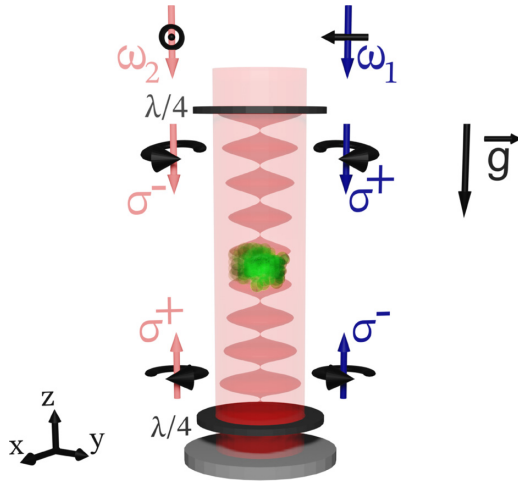


FIG. 6. Two laser beams at frequencies ω_1 and ω_2 are overlapped with orthogonal linear polarizations. The beams pass through a first $(\lambda/4)$ -wave plate to obtain circular polarizations and are retro-reflected through a second $\lambda/4$ plate. This setup creates two vertical optical lattices corresponding to the σ^+/σ^+ and σ^-/σ^- pairs, with each one pairing both frequencies.

for the considered interaction times. However, for a given diffraction order, we have seen that there is an optimal γ_{\max} . Therefore, for a given laser intensity, it is possible to find an optimal Δ value which minimizes the spontaneous emission [63]. The laser is split into two paths passing through two double-pass acousto-optic modulators (AOMs) controlling the frequency difference and phase of the optical lattice. They are recombined on crossed polarization in a polarization-maintaining fiber. A last AOM controls the amplitude of both beams up to 150 mW and thus allows the temporal pulse shaping of the optical lattice. The two beams are finally collimated with a Gaussian waist $w_0 = 4$ mm and polarized with orthogonal circular polarizations. The beams are then retroreflected along the vertical axis after passing through a quarter-wave plate. This configuration creates two quasistanding waves for each circular polarization with opposite velocities $\pm\Delta\omega/2k$ and opposite phases.

For large enough initial velocity of the atoms $v_0 \gg v_r$, only one of the two lattices can fulfill the Bragg condition at a time. The other one is Doppler shifted off resonance and does not interact with the atoms. In practice, the initial velocity is acquired by letting the atom fall under gravity for 6 ms before the optical lattice is turned on. To ensure the Bragg condition is satisfied for long interaction times or complex pulse sequences, the constant gravity acceleration is compensated by a constant frequency ramp on one of the two beams [see Eq. (4)].

The populations in different momentum states are measured by time-of-flight fluorescence imaging after 20 ms of free fall. The spatial separation corresponding to a momentum separation of $2\hbar k$ equals around $230 \mu\text{m}$, which is larger than the typical cloud size of $\simeq 60 \mu\text{m}$ (radius at $\frac{1}{\sqrt{e}}$). The images are integrated along the direction orthogonal to the diffracting lattice, and the resulting profiles are fitted with a sum of regularly separated Gaussians corresponding to each momentum state. The relative population in each state is taken to be the

integral of the corresponding Gaussian divided by the total integrated signal.

B. Quasi-Bragg diffraction

The high-order Bragg diffraction in the quasi-Bragg regime is illustrated in Fig. 7. We have performed measurements of the populations in the different momentum states after a pulse of order $n = 3$ with a peak two-photon Rabi frequency $\gamma_{\max} = 3.3$. The pulse duration σ is scanned between $0.05\omega_r^{-1}$ and $1.1\omega_r^{-1}$. The distribution of the population over the different momentum states is well reproduced by the numerical simulation including the velocity selection effect for long pulses. The very good agreement between the data and the simulation does not rely on any data adjustment. The simulation needs only two parameters which are independently measured: the atomic velocity dispersion $\sigma_{\bar{v}}$, which is measured by time of flight, and the optical power P allowing a calculation of the two-photon Rabi frequency γ_{\max} (see Appendix A). In addition the calculated γ_{\max} is compared to the first-order Rabi oscillation with rectangular pulses.

The SP and LP regimes are still distinguishable with a finite-velocity-dispersion ensemble. Landau-Zener losses are significant for short pulses ($\sigma < 0.4\omega_r^{-1}$) and completely vanish for longer pulses. The velocity dispersion has a major impact in the LP regime, reducing the oscillation amplitude of the populations of the Bragg states as the spectral width of the pulse becomes narrower. In order to minimize the velocity selection and to address the whole atomic velocity distribution, one would like to use a pulse that is as short as possible. However, a very short pulse induces Landau-Zener losses and associated diffraction phases which degrade the interferometer performances. Therefore, a trade-off between the velocity selection and Landau-Zener losses is needed. It is highly dependent on the shape of the lattice pulse and on the velocity dispersion of the atomic source. The Gaussian shape pulses studied here are commonly used to reduce the spectral width of the pulse and thus the Landau-Zener losses, but they do not take full advantage of the available laser power to drive Rabi oscillations. One could think to use smooth edge functions with a larger pulse area [34] for the same γ_{\max} value to manage a better trade-off: an example of such a pulse is the ‘‘tanh pulse.’’ A lower velocity dispersion, achieved by velocity selection or δ -kick collimation techniques [70], gives more room between short-pulse Landau-Zener losses and long-pulse spectral narrowing.

The limited laser power and the finite velocity dispersion allow us to achieve a mirror pulse efficiency above 70% up to order $n = 6$ (see Fig. 12). Such an efficiency ensures good fringe visibility for three-pulse interferometers. However, it corresponds to pulse durations in the SP regime where losses are not negligible and diffraction phases are not trivial and are hard to control to a metrological level.

In order to study the impact of this choice in the quasi-Bragg regime on the interferometer signal we first compare the performances of individual mirror pulses in the SP or LP regime for Bragg order up to $n = 5$. Figure 8 shows how the population distributes over the different momentum states, including unwanted states, after the mirror pulses. Here, the LP pulses correspond to $\theta_R = 3\pi$, which matches the com-

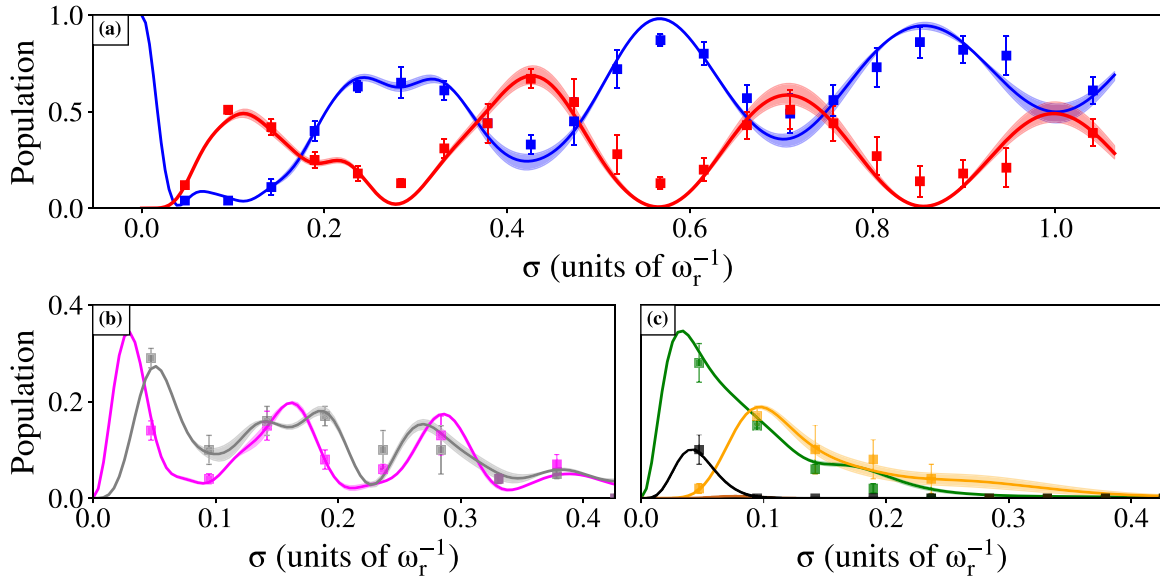


FIG. 7. Comparison of the measured and calculated relative populations of the various momentum states as a function of σ for a quasi-Bragg diffraction of order $n = 3$. The peak two-photon Rabi frequency is $\gamma_{\max} = 3.3$. (a) The relative populations in the different momentum states are plotted in blue and red for the two Bragg states $|0\hbar k\rangle$ and $|6\hbar k\rangle$, respectively. (b) Relative population in the inner states (pink: $|2\hbar k\rangle$, gray: $|4\hbar k\rangle$). (c) Relative population in the outer states (black: $| -4\hbar k\rangle$, green: $| -2\hbar k\rangle$, yellow: $|8\hbar k\rangle$). Each experimental point is an average of 10 measurements, and the error bar is the statistical shot-to-shot error. The solid lines are the results of the numerical simulation for a velocity dispersion corresponding to $0.32 \pm 0.05v_r$. The experimental uncertainty on the velocity dispersion is shown as the shading around the simulated populations.

promises illustrated in Fig. 5, while the SP pulses correspond to $\theta_R = \pi$ for the same γ_{\max} . For example, in the $n = 3$ case illustrated in Fig. 7, the LP mirror pulse duration is $\sigma \simeq 0.42\omega_r^{-1}$, and the SP mirror pulse duration is $\sigma \simeq 0.10\omega_r^{-1}$.

The LP pulses conserve the major part of the population in the two Bragg states, but the transfer efficiency is limited and decreases as the velocity selectivity increases with the Bragg

order. On the contrary, the SP pulses perform high efficiencies restricted to the two-Bragg states $\frac{P_n}{P_0+P_n}$, despite a significant loss of atoms in the unwanted states. These two different kinds of losses have different impacts on the interferometer signal, which will be discussed in the next section. The drop in transfer efficiency for $n = 5$ is due to the limited laser power, which prevents us from finding the optimal pulse parameters for such a high order.

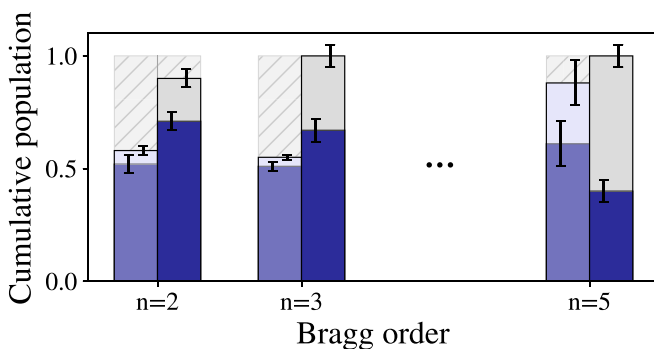


FIG. 8. Population distribution after a mirror pulse in the SP regime (left bars) and in the LP regime (right bars). The dark (light) color bar area stands for the transferred fraction P_n in $|2n\hbar k\rangle$ (non-transferred fraction P_0 in $|0\hbar k\rangle$). The hatched areas quantify the fraction of atoms lost in the unwanted states. The error bars are standard deviations over 10 realizations. The cumulative height of the two colored areas indicates the fraction of atoms detected and used for the calculation of the relative population at the output of the interferometer. The efficiencies restricted to the two-Bragg states $\frac{P_n}{P_0+P_n}$ for the SP pulses (LP) are 90% (79%) for $n = 2$, 93% (67%) for $n = 3$, and 70% (40%) for $n = 5$.

C. Quasi-Bragg atom interferometer

We perform Mach-Zehnder-type three-pulse interferometers. In the usual two-level picture, relevant for Raman pulses or in the deep Bragg regime, the beam-splitter pulses correspond to $\theta_R = \pi/2$, and the central mirror pulse corresponds to $\theta_R = \pi$. However, in the quasi-Bragg regime, such low Rabi phases would have been obtained for short pulses leading to large Landau-Zener losses. In the following experiments, the beam splitters are realized with longer pulses, giving $\theta_R = 3\pi/2$ [see Fig 3(a)]. This value corresponds to a pulse at the frontier between the SP and LP regimes and thus represents a compromise between Landau-Zener losses and velocity selection.

We build interferometers up to $n = 5$ with the different central mirror pulses studied in Fig. 8. The interferometer phase is scanned by adding a phase shift $\Delta\varphi$ to one of the laser beams forming the lattice prior to the last Bragg pulse. Figures 9(a) and 9(b) show, as an example, the interference fringes for $n = 3$ for the two configurations of the central pulse. The population in one of the output ports is normalized to the population in the two main output ports and is fitted with a sine function, as expected for a two-path interferometer. The

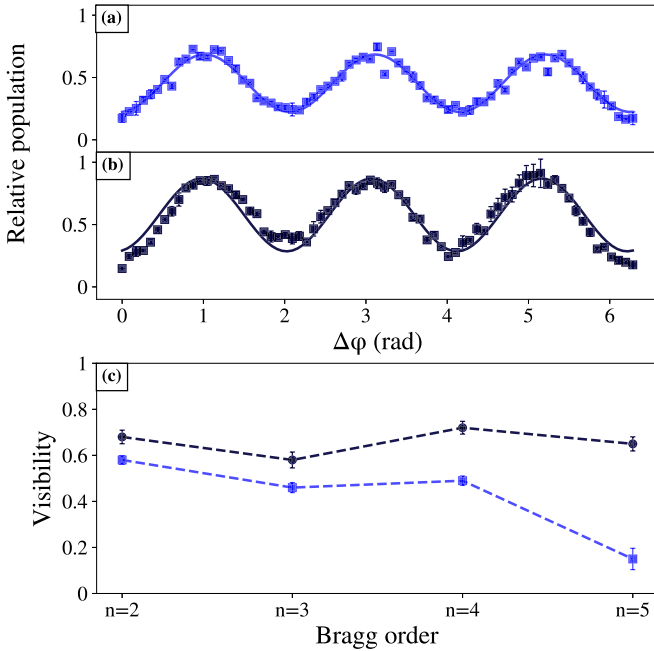


FIG. 9. Sample interference patterns for mirror pulses in the (a) LP and (b) SP regimes for $n = 3$. We show the relative atom number in one of the two main output ports normalized by the population in both main ports as a function of the phase shift. Error bars are standard deviations over three realizations. The solid lines are sinusoidal fits to the data. (c) Fitted visibility in the SP regime (black circles) and in the LP regime (blue squares) as a function of the Bragg order. Error bars for SP interferometers reflect the distortion of the signal and the mismatch with the pure sine model.

interrogation time between two pulses is small ($T = 1$ ms) in order to minimize the effect of environmental perturbations, such as vibrations and to focus on the impact of the diffraction losses on the interferometer signal. In addition, for interferometers with large arm separations, the atoms experience different optical fields on each arm. Therefore, the absolute ac Stark shift averages unevenly on each arm, which reduces the visibility. However, for the interrogation time T considered in this paper, the separation is small enough to ignore this effect. In addition, for larger arm separation, it is possible [55] to compensate the mean ac Stark shift by using a laser with a supplementary frequency corresponding to a detuning of a sign opposite that of the Bragg diffraction beams. The relative intensity of this supplementary frequency beam must be adjusted with respect to the Bragg beams to cancel the mean ac Stark shift.

In the LP regime [see Fig. 9(a) for $n = 3$], the fringe pattern stays very close to a pure sine. This pattern indicates that all atoms are measured in one of the two Bragg states with vanishing population in the unwanted states. The fitted visibilities for LP interferometers are plotted as blue points in Fig. 9(c). The fringe visibility decreases with the Bragg order n as the velocity bandwidth of the diffraction pulse decreases with n , so that a larger fraction of the population remains in the initial state and does not contribute to the fringe signal. The finite available laser power limits the Bragg order to $n = 5$ with a fitted visibility around 15%.

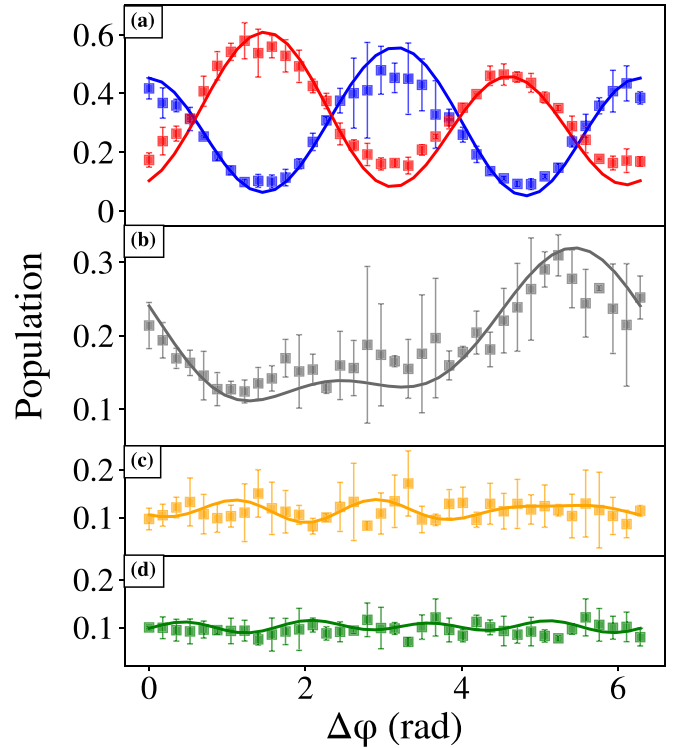


FIG. 10. Fringe patterns for $n = 2$. The pulses parameters are $\gamma_{\max} = 1.75$, $\sigma = 0.46\omega_r^{-1}$ for the beam-splitter pulses ($\theta_R = 5\pi/2$) and $\sigma = 0.15\omega_r^{-1}$ for the mirror pulse ($\theta_R \sim \pi$). The multiport nature of Bragg diffraction leads to distorted fringe patterns. The momentum states depicted are (a) the two Bragg states, (b) the inner state, and (c) and (d) the two outer states. Each experimental data point is an average of three points, and the error bar is the standard deviation. Solid lines are the results of numerical simulation for a velocity dispersion of $0.32v_r$.

The SP regime offers the possibility of addressing a broader velocity distribution which contributes to keeping an almost constant visibility up to order $n = 4$ [see black circles in Fig. 9(c)]. The degraded performance for $n = 5$ is also due to limited laser power. The improved visibility is explained by the inefficiency of the pulses which populate unwanted momentum states that are filtered out by the normalization and do not enter the estimation of the plotted relative population. Therefore, the total number of atoms contributing to the interferometer signal is reduced with respect to the LP counterpart (see Fig. 8). In addition, the population in the unwanted states leads to large diffraction phases and parasitic interferometric paths that distort the fringe patterns. In this regime, the interferometer is no longer a two-path interferometer leading to a degraded phase estimation [see Fig. 9(b)].

The multiport nature of the interferometer in the quasi-Bragg regime plays an already significant role for order $n = 2$, as shown in Fig. 10. It shows the populations in all the different measurable output ports normalized to the total number of detected atoms. The experimental data are compared with our numerical calculation.

As expected for $n = 2$ order pulses, the two main output ports oscillate with a period π as the laser phase shift $\Delta\phi$ is imprinted twice during the diffraction event [see Fig. 10(a)].

The fringe pattern is strongly distorted, and this distortion is obviously related to the strong modulation of the population of the inner state, which is unique in the $n = 2$ case. This behavior is a typical signature of interferometers involving more than two paths and leads to a systematic error of the phase measurement since the response function strongly differs from the expected sine shape. The populations in the outer states are non-negligible, but their modulation is much weaker, and they do not have a significant impact on the phase measurement for the present experimental parameters.

Spurious interferometers have been observed in dual interferometers from the residual errors of a Lissajou fitting [62]. In particular, the authors observed a “magic” pulse duration minimizing the errors on the phase extraction. We think the effect is related to a minimum of unwanted momentum states populated during the $\pi/2$ pulses in the SP regime. We believe that our direct observations of the fringes on each interferometer’s outputs will guide the theories needed to read the phase taking into account multiport features [71].

IV. CONCLUSIONS

We have investigated atom diffraction and interferometry of a BEC by a standing light wave in the quasi-Bragg regime up to the sixth Bragg order. We have shown simulations with no adjusted parameters, in good agreement with experimental results for arbitrary pulse-length regimes (short and long pulses) and initial velocity dispersion. In particular, we have modeled with very good agreement with the experiment all the momentum states involved in the diffraction process: Bragg states and nonadiabatic losses. Our work points out the required size of the momentum basis for accurate calculations of the diffraction process. By matching simulations and experiments we provide a quantitative understanding of the inherent diffraction phase shifts and multiport features of LMT interferometers based on quasi-Bragg diffraction. We confirmed the link between diffraction phases and the nonadiabatic losses, and our simulations anticipate diffraction phase shifts of up to several tens of milliradians. We demonstrated an optimal diffraction efficiency at the border between the SP and LP regimes for a Rabi phase $\theta_R \geq \pi$. A higher Rabi phase, i.e., higher $(\sigma, \gamma_{\max})_{\text{opt}}$, would lead to a similar diffraction efficiency limited by the velocity selection and a reduced diffraction phase but might impact the effects scaling in $\gamma_{\max}\sigma$ such as the ac Stark shift and spontaneous emissions. We have also demonstrated interferometer fringes with phase-controlled interferometers up to $n = 5$. Therefore, we were able to observe the impact of the multipath interferences directly on the fringe’s signal for each interferometer’s outputs. The insight gained from these investigations should guide the development of new methods for better optimization and estimation of multiport interferometers.

ACKNOWLEDGMENTS

We acknowledge B. Decamps, J. Alibert and M. Bordoux for their contributions in the early stages of the experimental setup. We thank J. P. Gauyacq, N. Gaaloul, K. Hammerer, and J.-N. Siemß for fruitful discussions. This research was supported by Grant No. ANR-19-CE47-0002.

APPENDIX A: LATTICE-DEPTH MEASUREMENT Ω

Bragg scattering can be described as a multiphoton Raman process between momentum states. Each elementary two-photon Raman process couples momentum states in the same internal ground states $|F_g, m_{F_g}\rangle$ through an intermediate excited state in a different internal state $|F_e, m_{F_e}\rangle$. The single-photon Rabi frequencies between a ground state and an intermediate state are denoted $\Omega_{|e\rangle}$. The excited states have a lifetime $1/\Gamma$. For a large detuning ($\Delta \gg \Omega_{|e\rangle}, \Gamma$) from intermediate level $|e\rangle$ (see Fig. 1), the system can be described as an effective two-level system by adiabatically eliminating the intermediate level $|e\rangle$. The effective Rabi frequency between two momentum states is given by summing over all possible intermediate states:

$$\Omega = \sum_{|e\rangle} \frac{\Omega_{|e\rangle}^2}{2\Delta}. \quad (\text{A1})$$

In the electric-dipole approximation, $\Omega_{|e\rangle}$ is proportional to the product of the electric field amplitude by the matrix element of the dipole operator. Using the Wigner-Eckart theorem, we factor out the reduced matrix element and Clebsch-Gordan coefficient.

$$\Omega_{|e\rangle} = E_0 \sqrt{\frac{3\epsilon_0\lambda^3\Gamma}{2\pi^2\hbar}} \sqrt{(2F_e + 1)(2F_g + 1)} \\ \times \begin{Bmatrix} J_e & 1 & J_g \\ F_g & I & F_e \end{Bmatrix} \begin{pmatrix} F_e & 1 & F_g \\ -m_{F_e} & q & m_{F_g} \end{pmatrix}. \quad (\text{A2})$$

In practice, we use the D_2 lines of ^{87}Rb , corresponding to a wavelength $\lambda = 780.1$ nm, and a natural linewidth $\Gamma = 2\pi \times 6.1$ MHz. ϵ_0 is the vacuum permittivity. The laser field polarization is given in standard components $q = \pm 1, 0$. The amplitude of the electric field corresponding to a single-photon transition is evaluated from the power P and the Gaussian beam waist w_0 :

$$E_0 = \frac{2}{w_0} \sqrt{\frac{P}{\pi c \epsilon_0}}. \quad (\text{A3})$$

In our experimental setup, the retroreflected configuration leads to two optical lattices with orthogonal polarization. The optical power for each lattice’s arm is recycled by the retroreflection. Therefore, P is the optical power measured in the incident laser beam for each frequency ω_1 and ω_2 (i.e., the total incident optical power is $2P$).

All the data reported in this paper are measured with atoms prepared in the ground state ($J_g = 1/2, F_g = 1, m_{F_g} = 0$) and the optical lattice with the circular polarization σ_- ($q = -1$ in standard components). Therefore, only two intermediate states $|e\rangle$ are coupled: $J_e = 1/2, F_e = 1, 2, m_{F_e} = -1$.

The effective two-photon Rabi frequency [Eq. (A1)] is a central parameter in the atom diffraction with an optical lattice. In order to determine Ω , we measured the Rabi oscillations between the two diffracted states with a rectangular-pulse first-order Bragg diffraction in the Bragg regime (Fig. 11). We obtain good agreement between the measured and calculated Ω .

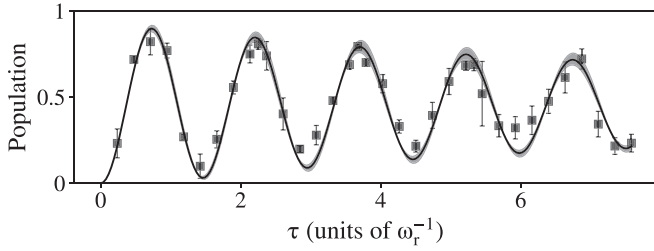


FIG. 11. Evolution of the diffracted Bragg state for a resonance condition for Bragg order $n = 1$. The temporal shape of the envelope of the lattice is rectangular.

APPENDIX B: TRUNCATION OF THE MOMENTUM BASIS USED FOR THE NUMERICAL MODEL

We showed in Fig. 2 that the dynamics of high-order Bragg diffraction requires us to consider a sufficiently large momentum basis. For example, we compare the measured diffraction probability for a quasi-Bragg order $n = 6$ to its numerically predicted value for different basis truncations. Figure 12 presents this comparison for a large range of the pulse duration σ . For $m = 0$, meaning that the basis contains only the two Bragg states and the inner states in between, the numerical result fails to estimate both the amplitude and the frequency of the population oscillation. Considering two outer states ($m = 1$) increases the agreement with the experimental results. The complex dynamics is properly captured for $m \geq 2$. The overlap of the two curves for $m = 2$ and $m = 3$ confirms the convergence of the simulation.

We numerically solve the system of differential equations using the `SCIPY.INTEGRATE` package of `PYTHON`. The computational cost rapidly increases with the basis size, especially when considering a nonzero velocity dispersion. It is thus interesting to find a criterion giving the minimal value m_0 of outer states that has to be considered for a given quasi-Bragg order n .

A first naive energetic criterion is related to the fact that all states $|2l\hbar k\rangle$ between the two Bragg states ($l \in [0, n]$) are naturally included in the calculation. The model should then

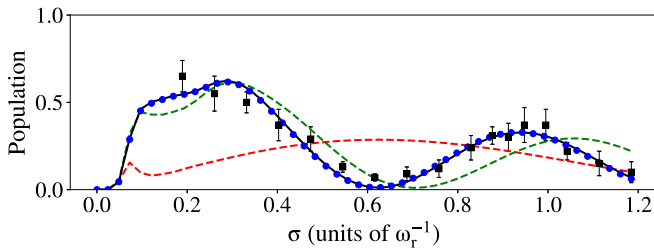


FIG. 12. Population in $|12\hbar k\rangle$ state for $n = 6$ and $\gamma_{\max} = 6.25$ as a function of the pulse duration. Black squares are the experimental measurements. Error bars are standard deviations on 10 measurements. The experimental data are compared with numerical simulation results for the corresponding pulse parameters and atomic velocity dispersion for various m values. The dashed lines are simulation results for $m = 0$ (red) and $m = 1$ (green). The black solid line is the result for $m = 2$ and overlaps with blue dotted line corresponding to $m = 3$.

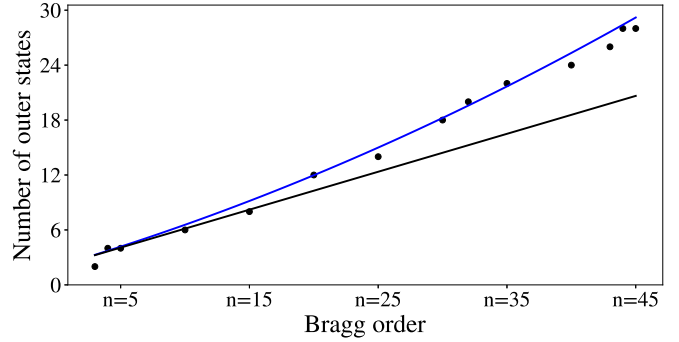


FIG. 13. Comparison of the minimum required number of outer states as a function of the quasi-Bragg order n . Black dots are the results of a convergence test $2m_c$. The solid black line is the lower bound criterion $2m_0$ derived from the energetic argument. The blue solid line is an empirical correction to the criterion adding a n^2 contribution [Eq. (B3)]. The lines correspond to the nonrounded analytical formulas for $2m_0$ and $2m_0^{\text{emp}}$.

at least consider outer states down to $|-2(m_0)\hbar k\rangle$ so that $\delta_{-m_0} \geq \max_{l \in [0, n]} |\delta_l|$. Note that the exact same criterion is obtained considering outer states up to $|2(n + m_0)\hbar k\rangle$ since the diagonal term δ_l is symmetric. When the Bragg condition is realized for the quasi-Bragg order n , the maximum detuning for inner states reads

$$\max_{l \in [0, n]} |\delta_l| = \begin{cases} |\delta_{n/2}| = n^2/4 & \text{if } n \text{ is even,} \\ |\delta_{(n-1)/2}| = (n^2 - 1)/4 & \text{if } n \text{ is odd.} \end{cases} \quad (\text{B1})$$

Solving the equality and rounding to the next integer give the criterion for m_0 :

$$m_0 = \begin{cases} \lceil \frac{1}{2}n(\sqrt{2} - 1) \rceil & \text{if } n \text{ is even,} \\ \lceil \frac{1}{2}n(\sqrt{2 - \frac{1}{n^2}} - 1) \rceil & \text{if } n \text{ is odd,} \end{cases} \quad (\text{B2})$$

where $\lceil x \rceil$ is the ceiling function that rounds x to the least integer greater than or equal to x .

In practice, for $n > 3$, the $1/n^2$ term for odd quasi-Bragg order does not affect the rounded value for m_0 . We thus take $m_0 = \lceil \frac{1}{2}n(\sqrt{2} - 1) \rceil$ as a lower bound for m .

This criterion is compared to a convergence test of the truncation of the calculation basis performed in the case of zero velocity dispersion. The quantity of interest is the peak Rabi frequency γ_{\max} that gives a perfect mirror pulse (diffraction probability $>99\%$) with the shortest pulse length. This quantity varies with m and converges to a constant value for $m > m_c$. Figure 13 shows a comparison between the values of m_c (black dots) and the previously derived criterion m_0 (black line) for different quasi-Bragg orders n .

The minimum required number of outer states is well predicted by the criterion m_0 up to a quasi-Bragg order $n \simeq 10$. It appears that it does not capture the n^2 term relevant for high n [63]. We propose a modified criterion m_0^{emp} including a minimal fitted n^2 term that reproduces the convergence test results:

$$m_0^{\text{emp}} = \lceil \frac{1}{2}n(\sqrt{2} - 1) + 1 + An^2 \rceil, \quad (\text{B3})$$

where $A \approx 2 \times 10^{-3}$.

This analytical criterion is based on a simple energetic argument and compared to zero-velocity calculations. It gives a lower bound for the number of outer states that has to be included to accurately reproduce the dynamics. For rele-

vant experimental parameters, with large velocity dispersion and/or high peak two-photon Rabi frequency, one might have to run a dedicated convergence test to ensure that all the relevant off-resonant couplings are taken into account.

-
- [1] P. L. Kapitza and P. A. M. Dirac, The reflection of electrons from standing light waves, *Math. Proc. Cambridge Philos. Soc.* **29**, 297 (1933).
- [2] D. L. Freimund, K. Aflatooni, and H. Batelaan, Observation of the Kapitza–Dirac effect, *Nature (London)* **413**, 142 (2001).
- [3] S. Altshuler, L. M. Frantz, and R. Braunstein, Reflection of Atoms from Standing Light Waves, *Phys. Rev. Lett.* **17**, 231 (1966).
- [4] E. Arimondo, H. Lew, and T. Oka, Deflection of a Na Beam by Resonant Standing-Wave Radiation, *Phys. Rev. Lett.* **43**, 753 (1979).
- [5] P. E. Moskowitz, P. L. Gould, S. R. Atlas, and D. E. Pritchard, Diffraction of an Atomic Beam by Standing-Wave Radiation, *Phys. Rev. Lett.* **51**, 370 (1983).
- [6] A. F. Bernhardt and B. W. Shore, Coherent atomic deflection by resonant standing waves, *Phys. Rev. A* **23**, 1290 (1981).
- [7] M. Marte and S. Stenholm, Multiphoton resonances in atomic Bragg scattering, *Appl. Phys. B* **54**, 443 (1992).
- [8] P. L. Gould, G. A. Ruff, and D. E. Pritchard, Diffraction of Atoms by Light: The Near-Resonant Kapitza-Dirac Effect, *Phys. Rev. Lett.* **56**, 827 (1986).
- [9] S. Dürr, S. Kunze, and G. Rempe, Pendellösung oscillations in second-order Bragg scattering of atoms from a standing light wave, *Quantum Semiclassical Opt.* **8**, 531 (1996).
- [10] S. Dürr and G. Rempe, Acceptance angle for Bragg reflection of atoms from a standing light wave, *Phys. Rev. A* **59**, 1495 (1999).
- [11] M. Wilkens, E. Schumacher, and P. Meystre, Band theory of a common model of atom optics, *Phys. Rev. A* **44**, 3130 (1991).
- [12] C. Champenois, M. Büchner, R. Delhuille, R. Mathevet, C. Robilliard, C. Rizzo, and J. Vigué, Atomic diffraction by a laser standing wave: Analysis using Bloch states, *Eur. Phys. J. D* **13**, 271 (2001).
- [13] C. Keller, J. Schmiedmayer, A. Zeilinger, T. Nonn, S. Dürr, and G. Rempe, Adiabatic following in standing-wave diffraction of atoms, *Appl. Phys. B* **69**, 303 (1999).
- [14] S. Gupta, A. E. Leanhardt, A. D. Cronin, and D. E. Pritchard, Coherent manipulation of atoms with standing light waves, *C. R. Acad. Sci. Ser. IV, Phys.* **2**, 479 (2001).
- [15] P. J. Martin, B. G. Oldaker, A. H. Miklich, and D. E. Pritchard, Bragg Scattering of Atoms from a Standing Light Wave, *Phys. Rev. Lett.* **60**, 515 (1988).
- [16] S. M. Dickerson, J. M. Hogan, A. Sugarbaker, D. M. S. Johnson, and M. A. Kasevich, Multiaxis Inertial Sensing with Long-Time Point Source Atom Interferometry, *Phys. Rev. Lett.* **111**, 083001 (2013).
- [17] A. Gauguet, B. Canuel, T. Lévêque, W. Chaibi, and A. Landragin, Characterization and limits of a cold-atom Sagnac interferometer, *Phys. Rev. A* **80**, 063604 (2009).
- [18] B. Fang, I. Dutta, P. Gillot, D. Savoie, J. Lautier, B. Cheng, C. L. Garrido Alzar, R. Geiger, S. Merlet, F. Pereira Dos Santos, and A. Landragin, Metrology with atom interferometry: Inertial sensors from laboratory to field applications, *J. Phys.: Conf. Ser.* **723**, 012049 (2016).
- [19] Y. Bidet, N. Zahzam, C. Blanchard, A. Bonnin, M. Cadoret, A. Bresson, D. Rouxel, and M. F. Lequentrec-Lalancette, Absolute marine gravimetry with matter-wave interferometry, *Nat. Commun.* **9**, 627 (2018).
- [20] Z.-K. Hu, B.-L. Sun, X.-C. Duan, M.-K. Zhou, L.-L. Chen, S. Zhan, Q.-Z. Zhang, and J. Luo, Demonstration of an ultrahigh-sensitivity atom-interferometry absolute gravimeter, *Phys. Rev. A* **88**, 043610 (2013).
- [21] C. Freier, H. Hauth, V. Schkolnik, B. Leykauf, M. Schilling, H. Wziontek, H.-G. Scherneck, J. Müller, and A. Peters, Mobile quantum gravity sensor with unprecedented stability, *J. Phys.: Conf. Ser.* **723**, 012050 (2016).
- [22] G. Rosi, F. Sorrentino, L. Cacciapuoti, M. Prevedelli, and G. M. Tino, Precision measurement of the Newtonian gravitational constant using cold atoms, *Nature (London)* **510**, 518 (2014).
- [23] L. Morel, Z. Yao, P. Cladé, and S. Guellati-Khélifa, Determination of the fine-structure constant with an accuracy of 81 parts per trillion, *Nature (London)* **588**, 61 (2020).
- [24] P. A. Altin, M. T. Johnsson, V. Negnevitsky, G. R. Dennis, R. P. Anderson, J. E. Debs, S. S. Szigeti, K. S. Hardman, S. Bennetts, G. D. McDonald, L. D. Turner, J. D. Close, and N. P. Robins, Precision atomic gravimeter based on Bragg diffraction, *New J. Phys.* **15**, 023009 (2013).
- [25] B. Décamps, J. Vigué, A. Gauguet, and M. Büchner, Measurement of the 671-nm tune-out wavelength of ^7Li by atom interferometry, *Phys. Rev. A* **101**, 033614 (2020).
- [26] J. Gillot, S. Lepoutre, A. Gauguet, J. Vigué, and M. Büchner, Measurement of the Aharonov-Casher geometric phase with a separated-arm atom interferometer, *Eur. Phys. J. D* **68**, 168 (2014).
- [27] J. Gillot, S. Lepoutre, A. Gauguet, M. Büchner, and J. Vigué, Measurement of the He-McKellar-Wilkens Topological Phase by Atom Interferometry and Test of Its Independence with Atom Velocity, *Phys. Rev. Lett.* **111**, 030401 (2013).
- [28] D. M. Giltner, R. W. McGowan, and S. A. Lee, Atom Interferometer Based on Bragg Scattering from Standing Light Waves, *Phys. Rev. Lett.* **75**, 2638 (1995).
- [29] D. M. Giltner, R. W. McGowan, and S. A. Lee, Theoretical and experimental study of the Bragg scattering of atoms from a standing light wave, *Phys. Rev. A* **52**, 3966 (1995).
- [30] A. E. A. Koolen, G. T. Jansen, K. F. E. M. Domen, H. C. W. Beijerinck, and K. A. H. van Leeuwen, Large-angle adjustable coherent atomic beam splitter by Bragg scattering, *Phys. Rev. A* **65**, 041601(R) (2002).
- [31] M. A. H. M. Jansen, K. F. E. M. Domen, H. C. W. Beijerinck, and K. A. H. van Leeuwen, Off-resonance atomic Bragg scattering, *Phys. Rev. A* **76**, 053629 (2007).
- [32] H. Müller, S.-W. Chiow, and S. Chu, Atom-wave diffraction between the Raman-Nath and the Bragg regime: Effective Rabi

- frequency, losses, and phase shifts, *Phys. Rev. A* **77**, 023609 (2008).
- [33] H. Müller, S.-W. Chiow, Q. Long, S. Herrmann, and S. Chu, Atom Interferometry with up to 24-Photon-Momentum-Transfer Beam Splitters, *Phys. Rev. Lett.* **100**, 180405 (2008).
- [34] D. Gochnauer, K. E. McAlpine, B. Plotkin-Swing, A. O. Jamison, and S. Gupta, Bloch-band picture for light-pulse atom diffraction and interferometry, *Phys. Rev. A* **100**, 043611 (2019).
- [35] J.-N. Siemß, F. Fitzek, S. Abend, E. M. Rasel, N. Gaaloul, and K. Hammerer, Analytic theory for Bragg atom interferometry based on the adiabatic theorem, *Phys. Rev. A* **102**, 033709 (2020).
- [36] S. Gupta, K. Dieckmann, Z. Hadzibabic, and D. E. Pritchard, Contrast Interferometry Using Bose-Einstein Condensates to Measure \hbar/m and α , *Phys. Rev. Lett.* **89**, 140401 (2002).
- [37] S.-W. Chiow, T. Kovachy, H.-C. Chien, and M. A. Kasevich, $102\hbar k$ Large Area Atom Interferometers, *Phys. Rev. Lett.* **107**, 130403 (2011).
- [38] B. Plotkin-Swing, D. Gochnauer, K. E. McAlpine, E. S. Cooper, A. O. Jamison, and S. Gupta, Three-Path Atom Interferometry with Large Momentum Separation, *Phys. Rev. Lett.* **121**, 133201 (2018).
- [39] J. Rudolph, T. Wilkason, M. Nantel, H. Swan, C. M. Holland, Y. Jiang, B. E. Garber, S. P. Carman, and J. M. Hogan, Large Momentum Transfer Clock Atom Interferometry on the 689 nm Intercombination Line of Strontium, *Phys. Rev. Lett.* **124**, 083604 (2020).
- [40] P. Cladé, S. Guellati-Khélifa, F. Nez, and F. Biraben, Large Momentum Beam Splitter Using Bloch Oscillations, *Phys. Rev. Lett.* **102**, 240402 (2009).
- [41] H. Müller, S.-W. Chiow, S. Herrmann, and S. Chu, Atom Interferometers with Scalable Enclosed Area, *Phys. Rev. Lett.* **102**, 240403 (2009).
- [42] J. E. Debs, P. A. Altin, T. H. Barter, D. Döring, G. R. Dennis, G. McDonald, R. P. Anderson, J. D. Close, and N. P. Robins, Cold-atom gravimetry with a Bose-Einstein condensate, *Phys. Rev. A* **84**, 033610 (2011).
- [43] G. D. McDonald, C. C. N. Kuhn, S. Bennetts, J. E. Debs, K. S. Hardman, M. Johnsson, J. D. Close, and N. P. Robins, $80\hbar k$ momentum separation with Bloch oscillations in an optically guided atom interferometer, *Phys. Rev. A* **88**, 053620 (2013).
- [44] M. Gebbe, J.-N. Siemß, M. Gersemann, H. Müntinga, S. Herrmann, C. Lämmerzahl, H. Ahlers, N. Gaaloul, C. Schubert, K. Hammerer, S. Abend, and E. M. Rasel, Twin-lattice atom interferometry, *Nat. Commun.* **12**, 2544 (2021).
- [45] T. Hensel, S. Loriani, C. Schubert, F. Fitzek, S. Abend, H. Ahlers, J. N. Siemß, K. Hammerer, E. M. Rasel, and N. Gaaloul, Inertial sensing with quantum gases: A comparative performance study of condensed versus thermal sources for atom interferometry, *Eur. Phys. J. D* **75**, 108 (2021).
- [46] J. Li, G. R. M. da Silva, W. C. Huang, M. Fouda, J. Bonacum, T. Kovachy, and S. M. Shahriar, High sensitivity multi-axes rotation sensing using large momentum transfer point source atom interferometry, *Atoms* **9**, 51 (2021).
- [47] R. H. Parker, C. Yu, W. Zhong, B. Estey, and H. Müller, Measurement of the fine-structure constant as a test of the standard model, *Science* **360**, 191 (2018).
- [48] S. Dimopoulos, P. W. Graham, J. M. Hogan, and M. A. Kasevich, Testing General Relativity with Atom Interferometry, *Phys. Rev. Lett.* **98**, 111102 (2007).
- [49] G. M. Tino, Testing gravity with cold atom interferometry: Results and prospects, *Quantum Sci. Technol.* **6**, 024014 (2021).
- [50] B. Canuel *et al.*, ELGAR—A European laboratory for gravitation and atom-interferometric research, *Classical Quantum Gravity* **37**, 225017 (2020).
- [51] P. W. Graham, J. M. Hogan, M. A. Kasevich, S. Rajendran, and R. W. Romani, Mid-band gravitational wave detection with precision atomic sensors, [arXiv:1711.02225](https://arxiv.org/abs/1711.02225).
- [52] M.-S. Zhan *et al.*, Zaiga: Zhaoshan long-baseline atom interferometer gravitation antenna, *Int. J. Mod. Phys. D* **29**, 1940005 (2020).
- [53] Y. A. El-Neaj *et al.*, Aedge: Atomic experiment for dark matter and gravity exploration in space, *EPJ Quantum Technol.* **7**, 6 (2020).
- [54] O. Garcia, B. Deissler, K. J. Hughes, J. M. Reeves, and C. A. Sackett, Bose-Einstein-condensate interferometer with macroscopic arm separation, *Phys. Rev. A* **74**, 031601(R) (2006).
- [55] T. Kovachy, P. Asenbaum, C. Overstreet, C. A. Donnelly, S. M. Dickerson, A. Sugarbaker, J. M. Hogan, and M. A. Kasevich, Quantum superposition at the half-metre scale, *Nature (London)* **528**, 530 (2015).
- [56] S. Dürr, T. Nonn, and G. Rempe, Origin of quantum-mechanical complementarity probed by a ‘which-way’ experiment in an atom interferometer, *Nature (London)* **395**, 33 (1998).
- [57] Rameez-ul-Islam, M. Ikram, M. Imran, and G.-Q. Ge, Entanglement and the paradox of untying the defining feature from a quantum entity, *Phys. Rev. A* **100**, 052122 (2019).
- [58] C. Champenois, M. Büchner, R. Delhuille, R. Mathevet, C. Robilliard, C. Rizzo, and J. Vigué, Matter neutrality test using a Mach-Zehnder interferometer, *The Hydrogen Atoms*, Vol. 570 (Springer, Berlin, Heidelberg, 2001), pp. 554–563.
- [59] A. Arvanitaki, S. Dimopoulos, A. A. Geraci, J. Hogan, and M. Kasevich, How to Test Atom and Neutron Neutrality with Atom Interferometry, *Phys. Rev. Lett.* **100**, 120407 (2008).
- [60] M. A. Hohensee, B. Estey, P. Hamilton, A. Zeilinger, and H. Müller, Force-Free Gravitational Redshift: Proposed Gravitational Aharonov-Bohm Experiment, *Phys. Rev. Lett.* **108**, 230404 (2012).
- [61] M. Büchner, R. Delhuille, A. Miffre, C. Robilliard, J. Vigué, and C. Champenois, Diffraction phases in atom interferometers, *Phys. Rev. A* **68**, 013607 (2003).
- [62] R. H. Parker, C. Yu, B. Estey, W. Zhong, E. Huang, and H. Müller, Controlling the multiport nature of Bragg diffraction in atom interferometry, *Phys. Rev. A* **94**, 053618 (2016).
- [63] S. S. Szigeti, J. E. Debs, J. J. Hope, N. P. Robins, and J. D. Close, Why momentum width matters for atom interferometry with Bragg pulses, *New J. Phys.* **14**, 023009 (2012).
- [64] C. V. Raman and N. S. Nagendra Nath, The diffraction of light by high frequency sound waves, *Proc. Indian Sci. A* **2**, 406 (1936).

- [65] W. R. Klein and B. D. Cook, Unified approach to ultrasonic light diffraction, *IEEE Trans. Sonics Ultrason.* **14**, 123 (1967).
- [66] T. K. Gaylord and M. G. Moharam, Thin and thick gratings: Terminology clarification, *Appl. Opt.* **20**, 3271 (1981).
- [67] M. Abramowitz and I. A. Stegun, *Handbook of Mathematical Functions with Formulas, Graphs, and Mathematical Tables*, 9th Dover printing (Dover, New York, 1964).
- [68] J. Meixner, F. W. Schäfke, and G. Wolf, *Mathieu Functions and Spheroidal Functions and Their Mathematical Foundations, Further Studies*, Vol. 837 (Springer, Berlin, Heidelberg, 1980).
- [69] S. N. Shevchenko, S. Ashhab, and F. Nori, Landau-Zener-Stückelberg interferometry, *Phys. Rep.* **492**, 1 (2010).
- [70] H. Müntinga *et al.*, Interferometry with Bose-Einstein Condensates in Microgravity, *Phys. Rev. Lett.* **110**, 093602 (2013).
- [71] N. Gaaloul (private communication).